Direct numerical simulation of a near-field particle-laden plane turbulent jet

Jianren Fan,[1,*] Kun Luo,[1] Man Yeong Ha,[2] and Kefa Cen[1]
[1]*Institute for Thermal Power Engineering and CE & EE, Zhejiang University, Hangzhou 310027, China*
[2]*School of Mechanical Engineering, Pusan National University, Pusan 609-735, Korea*
(Received 26 September 2003; published 11 August 2004)

The present study investigates the gas-particle two-phase flow in the turbulent plane jet by solving the two-dimensional and compressible flow fields numerically using direct-numerical-simulation technique. The flow fields are spatially developing, but we focus our study on the evolution of coherent vortex structures and dispersion patterns of particles in the near field at different Stokes numbers. The initial symmetric mode of flow changes its shape to the asymmetric mode after about three convection periods as the flow moves downstream. The concessive paring processes between two and three vortex structures are observed. The predicted mean velocity profiles show self-similar behavior and coincide well with previous experimental data. The profiles of turbulent intensity and Reynolds shear stress also display self-similar characteristics in the further downstream regions. The local-focusing phenomena of particles occur in the quasicoherent dispersion structure of particles. The higher density distribution at the outer boundary of large-scale vortex structure characterizes the dispersion pattern of particles at the Stokes numbers of order of unity. Furthermore, these particles disperse largely along the lateral direction and show the nonuniform distribution of concentration. For the particles at the Stokes number of 0.01, the dispersion along the lateral direction is considerable due to the small aerodynamics response time, but the particles are distributed evenly in the flow field. Particles at the Stokes numbers of 10 and 50 disperse much less along the lateral direction with the even density distribution. These results support the previous conclusions on the dispersion of particles in the free shear flows.

DOI: 10.1103/PhysRevE.70.026303 PACS number(s): 47.55.Kf

I. INTRODUCTION

The turbulent plane jet flow is the basic free turbulent shear flow and is formed from the interaction of vorticies with opposite signs in the shear layers. The characteristics of turbulent plane jet flow are not observed in the flow of either mixing layer or circular jet. Fundamental study on the coherent structures and flow dynamics in the plane jet will contribute to the deep understanding of turbulent flows. Moreover, the gas-particle two-phase flow in the turbulent plane jet has wide engineering applications in the fields of coal combustion, chemical reaction, and environmental control. The capability of predicting accurately the large-scale vortex structure and particle dispersion in the jet is of great significance in designing various engineering systems efficiently.

The single-phase flow in the turbulent plane jet has been widely studied experimentally and numerically over the past decades. Albertson *et al.* [1] and Miller and Commings [2] measured the mean-velocity profiles in the plane jet. Later, the hot-wire anemometry was used to measure the mean and fluctuating statistical quantities in the self-similar region of plane jet [3,4]. It was found that the initial inlet and external experimental conditions have a strong effect on the evolution of the plane jet flow fields. Goldschmidt and Bradshaw [5] measured the lateral correlation across the jet and obtained the quasiperiodical negative correlation of longitudinal velocity. The longitudinal velocity autocorrelation coefficient across the plane jet showed the negative lobes for large probe separations [4,6]. These results showed the existence of a large-scale, flapping motion in the self-similar planar turbulent jet. Based on their observation, it was concluded that the negative correlation was the result of large-scale structures in the jet, rather than a flapping motion [7]. Subsequently, these large-scale structures were suggested as a 2D, asymmetric, and von Karman-like vortex street [8]. The developing characteristics of the large-scale vortex structures in a naturally developing 2D plane jet were studied, and it was observed that the flow patterns were initially characterized by relatively strong symmetric modes, and then by an asymmetric pattern formed beyond the jet potential core [9]. Recently, Zhou, Pearson, and Antonia [10] compared temporal and spatial transverse velocity increments in a turbulent plane jet and suggested that the spatial transverse increments are less anomalous with respect to scaling than the temporal increments formed with the transverse velocity component.

Comparing with experimental results there are fewer numerical simulations of the plane jets. Dai, Kobayashi, and Taniguchi [11] simulated numerically a 3D evolving subsonic plane jet with a large eddy simulation model. Their mean velocity profiles were in good agreement with experimental results, but the self-similar turbulence intensities were distinctly higher. Stanley and Sarkar [12] carried out a direct numerical simulation on the 2D single-phase flow in the plane jet and reported some useful results and discussions.

As to the gas-particle two-phase turbulent jet flows, many researchers carried out both the experimental and numerical studies. Melville and Bray [13] investigated the two-phase turbulent jet flows and brought forward a model to characterize them. Chung and Troutt [14] simulated the particle dispersion in an axisymmetric jet using a discrete vortex element approach. The interesting results were reported and

*Corresponding author. Email address: fanjr@zju.edu.cn

the ratio of particle dispersion to fluid agreed well with experimental results. Hardalupas, Taylor, and Whitelow [15] investigated the velocity and particle flux characteristics of a turbulent particle laden jet and suggested the small effect of the mass mixture ratio on the particle concentration distribution. Yuu, Ikeda, and Umekage [16] directly simulated a gas-particle turbulent-free jet at the low Reynolds numbers. Their computational results of air and particle-turbulent characteristics are in accord with their LDA experimental data.

Recently, the linear instability of a two-way coupled particle-laden jet was examined [17]. It was found that the addition of particles can destabilize the flow at a small particle Stokes number, and the particles at Stokes numbers on the order of 1 correspond to the maximum flow stability. A large-eddy simulation model considering the effect of particles on subgrid-scale flows was also employed to investigate the gas-particle jet flow in the slit nozzle at the high Reynolds numbers [18], and the calculated results were in good agreement with their experimental results.

However, there are few studies to investigate the large-scale vortex structures and particle dispersion in the gas-particle two-phase flow in the plane turbulent jets at the moderately high Reynolds numbers. In addition, most of the studies mentioned above are based on the incompressible hypothesis for the gas phase. In this paper, we use the direct numerical simulation (DNS) method to study the vortex dynamic characteristics and the particle dispersion patterns in a 2D evolving and compressible gas-solid turbulent plane jet.

The main objective of this study is to show the nonlinear development of coherent structures and particle dispersion modes at different Stoke numbers in the near field of compressible plane jet flows. Some quantitative statistics of flow and particle fields are also made to reveal the two-phase flow characteristics. Many experimental results have showed that the plane jet is largely 2D near the nozzle within 20 widths of the jet nozzle. So, our present study is of significance both in theory and practice.

II. GOVERNING EQUATIONS AND NUMERICAL SCHEME

A. Flow field simulation

1. Flow configuration and boundary conditions

Figure 1 shows the schematic of computational domain and flow configuration for the gas-particle two-phase flow in the 2D plane jet considered in the present study. The high-speed stream velocity is U_1 and the coflow stream velocity is U_2. The convective velocity U_c is defined as $(U_1+U_2)/2$, the convective period T_c is X_l/U_c, and the mean convective Mach number M_c is $(U_1-U_2)/(c_1+c_2)=0.15$. The ratio of the nozzle width d to the initial momentum thickness δ_0 is 20. The initial flow Reynolds number Re, based on the nozzle width and the velocity difference between two streams, equals 4500.

It is well known that for the simulation of turbulent flows in an open, nonperiodic environment system, the use of proper artificial boundary conditions at the computational domain boundaries is very crucial to obtain more accurate

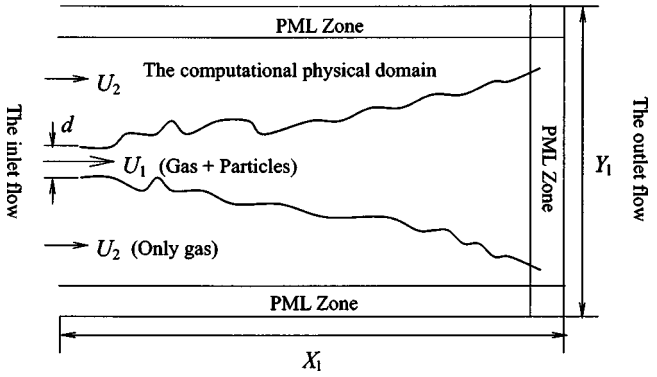

FIG. 1. Schematic of the computational domain and flow configuration for the gas-particle two-phase flow in the 2D plane jet.

simulation results. First, the large-scale vortex structures can leave the computational domain at the outflow boundary without being unphysically reflected. Second, the cross-stream entrainment in the flow field should be allowed. Third, the artificial boundary should allow the acoustic waves produced in the transition region to leave the domain without influencing the flow field by backward reflection. However, the accurate and efficient boundary conditions for the 3D Navier-Stokes equations have not yet been found. In practical simulations, it seems that combining the 1D nonreflecting boundary conditions [19] with the perfectly matched layer buffer-zone method could give reasonable results [12,20].

In this 2D simulation, the norreflecting boundary conditions and sponger layers [21–23] are added to the outflow and sidewall boundaries. At the jet inlet, outlet, and sidewall boundaries, the viscous boundary conditions [24] are also used. In addition, the typical top-hat inflow profile for the streamwise velocity is adopted. At the outflow boundary, the pressure correction [24,25] is performed. The whole computational domain is divided into a physical domain and three perfectly matched layer (PML) buffer zones. In the physical domain, uniform grid of $\Delta x=\Delta y=(1/15)d$ is used. While in the buffer zones, the stretched grid with 5% stretching ratio is employed. A total 257×315 computational grid system is utilized in the whole domain dimension of $X_l=17.656d$ and $Y_l=22.112d$.

2. Governing equations

In this study, we assume the gas phase fluid is an ideal and Newtonian gas. For this kind of compressible fluid, the nondimensional continuity, Navier-Stokes, energy, and ideal gas law equations in the physical domain are defined as follows:

$$\frac{\partial \rho}{\partial t}+\frac{\partial(\rho u_k)}{\partial x_k}=0 \tag{1}$$

$$\frac{\partial(\rho u_i)}{\partial t}+\frac{\partial(\rho u_i u_k)}{\partial x_k}=-\frac{\partial p}{\partial x_i}+\frac{1}{Re}\frac{\partial \tau_{ij}}{\partial x_j} \tag{2}$$

$$\frac{\partial p}{\partial t}+u_k\frac{\partial p}{\partial x_k}+\gamma p\frac{\partial u_k}{\partial x_k}=\frac{\gamma}{Pr\ Re}\frac{\partial}{\partial x_k}\left(\kappa\frac{\partial T}{\partial x_k}\right)+\frac{\gamma-1}{Re}\phi \tag{3}$$

$$p = \rho RT \tag{4}$$

where the shear stress tensor τ_{ij} in Eq. (2) and the viscous dissipation ϕ in Eq. (3) are expressed as

$$\tau_{ij} = \mu\left(\frac{\partial u_i}{\partial x_j} + \frac{\partial u_j}{\partial x_i}\right) - \frac{2}{3}\mu\frac{\partial u_k}{\partial x_k}\delta_{ij} \tag{5}$$

$$\phi = \tau_{ij}\frac{\partial u_i}{\partial x_j}. \tag{6}$$

To consider the three PML buffer zones shown in Fig. 1, the exponential damping terms are added to the above standard governing equations. Taking the continuity equation as an example, the continuity equation is modified as

$$\frac{\partial \rho}{\partial t} = -\frac{\partial(\rho u_k)}{\partial x_k} - \sigma(x,y)(\rho - \rho_0) \tag{7}$$

where ρ_0 is the target solution equal to the initial density value, and the absorbing coefficient σ is expressed as

$$\sigma(x,y) = \sigma_m(y)\left(\frac{x - x^*}{L_b}\right)^{\beta} \tag{8}$$

in which, x^* is the location of interface between the buffer zones and the interior physical domain $L_b(=x_{\max}-x^*)$ is the length of buffer zone, and σ_m used is 2 or 3. The added term can damp the density value to the specified target value across the buffer zones. This numerical algorithm was validated by comparing the predicted results with the linear stability theory, and the sensitivity of results to the variation of σ_m and β is little.

The similar terms are also added to the momentum and energy-conservation equations. At the sidewall boundaries, the streamwise velocity is damped to the coflow velocity, and the lateral velocity is damped to zero. For the outflow boundary, it seems valid to damp the streamwise velocity to the profile given in Ref. [3] and the lateral velocity to the profile given by $\partial U/\partial x + \partial V/\partial y = 0$.

3. Numerical scheme

The general requirements to simulate the turbulent flows using DNS technique efficiently are that the numerical scheme should provide the higher accuracy both in the spatial and temporal integration and also should be solved efficiently. To solve the governing equations for the fluid phase, the fourth-order compact finite difference schemes [26] are chosen to discretize the spatial derivatives in the interior mesh nodes, and the third-order compact finite difference schemes [27] are used at the boundary nodes. The stability of 3-4-3 derivative schemes was confirmed by applying this scheme to the linear 1D convection equation [28]. But these derivate evaluations are all done in the computational space on the uniform meshes. To get the derivative scheme working in the nonuniform meshes, these derivates are transformed to the physical space by utilizing the Jacobian of grid transformation.

The five-stage fourth-order Runge-Kutta integration scheme is adopted to integrate the Euler terms in the above governing equations, but the viscous and conduction terms are integrated in time by using the first-order Euler integration scheme. In addition, the nonuniform fourth-order compact filter originated from the uniform filter [26] is utilized to eliminate the high wave number errors.

B. Particle dispersion simulation

For the simulation of particle dispersion, several assumptions about the behavior of particles are made first [29]: (i) All particles are rigid spheres with identical diameter d_p and density ρ_p. (ii) The ratio of the material density of particle to fluid approximates to 2000. (iii) The fluid is considered as dilute two-phase flow. Thus the interaction between particles is neglected. (iv) The particles are ejected into the flow-field with even distribution at the nozzle and their velocity is equal to the local gas-phase velocity.

The largest ratio of the particle to fluid mass is about 7.54×10^{-5}, thus the effects of particles on fluid flow are also neglected. Because the larger velocity gradient in the free shear flow could exist at certain local areas, the Saffman lift force is considered in the present study, which was not taken into account ordinarily in previous simulations [30–32]. In the present work, the Stokes drag, Saffman lift, and gravity forces are considered as the main forces acting on a sphere. Thus, the equation to govern the particle motion is expressed as follows [33]:

$$m_p\frac{d\boldsymbol{V}}{dt} = \frac{\pi d_p^2}{8}C_D\rho_p|\boldsymbol{U}-V|(\boldsymbol{U}-V) + 1.61\upsilon^{\frac{1}{2}}\rho_g d_p^2(\boldsymbol{U}-\boldsymbol{V})\left|\frac{d\boldsymbol{U}}{dy}\right|^{\frac{1}{2}} + m_p g. \tag{9}$$

Then the dimensionless equation to govern the particle motion is defined as follows:

$$\frac{d\boldsymbol{V}}{dt} = \left(\frac{f}{\mathrm{St}} + \frac{9.66a\upsilon^{\frac{1}{2}}l_r\rho_g\left|\frac{d\boldsymbol{U}}{dy}\right|^{\frac{1}{2}}}{\pi d_p\rho_p u_r^2}\right)(\boldsymbol{U}-\boldsymbol{V}) + g \tag{10}$$

where $\boldsymbol{V}$ and $\boldsymbol{U}$ are the particle and fluid velocity vectors, respectively, at the same position. f is the modification factor for the Stokes drag coefficient, which can be described by $f=1+0.15\,\mathrm{Re}_p^{0.687}$ for $\mathrm{Re}_p\leqslant1000$. The particle Reynolds number $\mathrm{Re}_p=|\boldsymbol{U}-\boldsymbol{V}|d_p/\upsilon$, where d_p is the particle diameter and υ is the kinematical viscosity of the fluid. In this simulation, the particle Reynolds number is less than 1. St is the particle Stokes number, defined as $\mathrm{St}=(\rho_p d_p^2/18\mu)/(l_r/u_r)$ where ρ_p is the particle material density, μ is the fluid dynamics viscosity, l_r is the character length scale, and u_r is the character velocity scale. $\boldsymbol{g}$ is the nondimensional gravity acceleration vector defined as $\boldsymbol{g}=\boldsymbol{g}_b\,l_r/u_r^2$, where $\boldsymbol{g}_b$ is the standard gravity acceleration vector. Then the velocity and position of particles can be obtained by integrating Eq. (10), in which the fluid velocity $\boldsymbol{U}$ and modification factor f are treated as constants during the integration over the enough small time-step size. Since the flow velocity is obtained at every grid point by the numerical solution for the gas-phase governing equations, we use the fourth-order Lagrange inter-

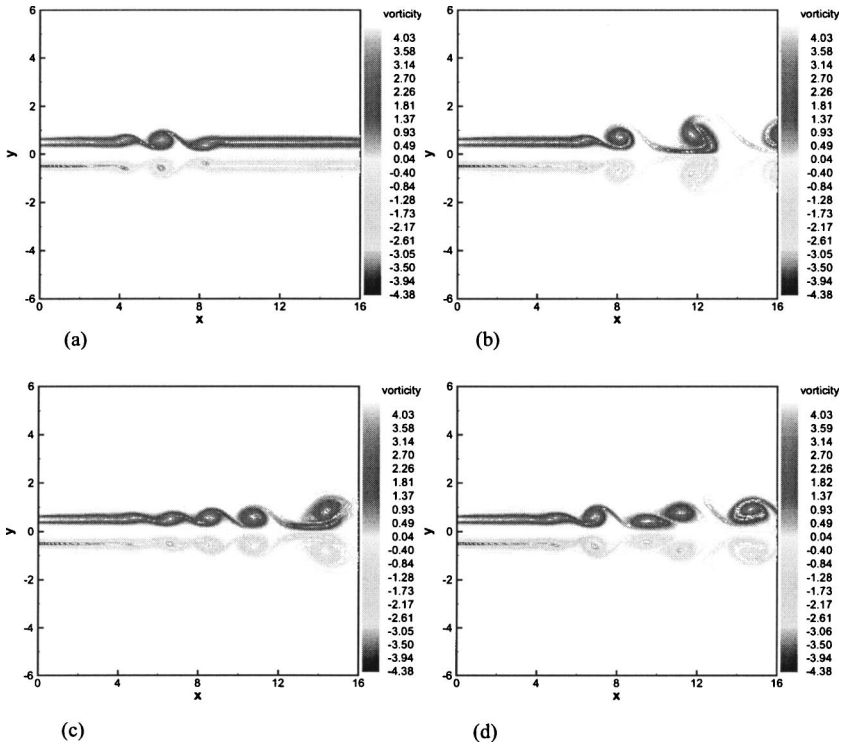

FIG. 2. (Color online) Evolution of vortex structures in the symmetric mode of flow fields at different nondimensional time t in the initial stage of jet flow. (a) $t=10.82$, (b) $t=28.82$, (c) $t=46.82$, and (d) $t=64.82$.

polating polynomials to determine the flow velocities at the particle positions.

In this work, the particle Stokes number varies in the range from 0.01 to 100. To demonstrate the typical dispersion pattern of particles, six kinds of particles corresponding to the Stokes numbers of 0.01, 0.1, 0.5, 5, 10, and 50 are chosen as tracers. For each case, 89 particles are ejected into the flow field at the inflow plane every five time steps. The nondimensional time step Δt is 0.018 and every convection period contains 1564 time steps. The flow field is calculated for 20 convection periods and as a result the total number of particles traced for each case is about 560 000.

III. NUMERICAL RESULTS AND DISCUSSION

A. Flow-field dynamics characteristics

1. Flow-field coherent structures evolution

Figure 2 shows the evolution of vortex structures in the flow field during the first three convection periods. x and y are the nondimensional coordinates scaled by nozzle width d. Only the section between $y=-6$ and $y=6$ along the lateral (y) direction is shown to display the vortex evolution more clearly. At the nondimensional time of $t=10.82$, the Kelvin-Helmholtz instability appears in the free shear layers because the mode corresponding to the natural frequency reaches its maximum. Then the roller vortex structures are formed at the position of $x=6.0$ in the free shear layers as shown in Fig. 2(a). These roller vortex structures develop symmetrically with opposite signs and march to the downstream direction at the speed of convection velocity U_c. But the vorticity at each side of shear layer has the same sign. The roller vortex at the upper or lower part comes together, corotates and eventually pairs to form a new, bigger roller as shown in Figs. 2(b)–2(d). During the pairing process, the interactions between two free-shear layers become strong, but the structures of flow field still maintain their symmetric mode. The length of potential core calculated from the present planar jet is 6, which is the same as the experimental result obtained from the natural 2D planar jet [9].

The transition of the flow structures from the symmetric to the asymmetric mode in the fully developed region is shown in Fig. 3. At $t=79.22$, the symmetric development mode of flow-field vorticity is destroyed, as shown in Fig. 3(a). After merging of shear layers, two side shear layers first begin to switch from the symmetric pattern to asymmetrical one at about the position of $x=10.0$, which is associated with the pairing process of roller vortex structures. The reason for this switch is that the interactions between two shear layers become stronger due to the consecutive pairing phenomena of roller vortex structures. When the subharmonic resonant forcing to the flow field becomes large enough, it wakens the asymmetric mode. As a result, the asymmetric mode in the jet shear layer starts to play the dominant role in the evolution of coherent structures. When the mode of fluid flow is asymmetric, the distribution of vortices is more complicated. There exists the single-roller vortex structure, pairing vortex structures with the same sign and combined vortex structures with the opposite sign, as shown in Figs. 3(b) and 3(c). As time goes on, the paired vortex structures continue to pair along with the vorticity amalgamation and destruction, and the opposite-sign vortex structures arrest each other to produce the arrangement of interlaced vortex structures, as shown in Fig. 3(d). It should be noted that the flow field switch from symmetric to asymmetric mode occurs at the downstream position where the shear layers are merged, but not at the upstream position where the self-preservation of flow fields starts. It occurs just at the position of $x=10.0$,

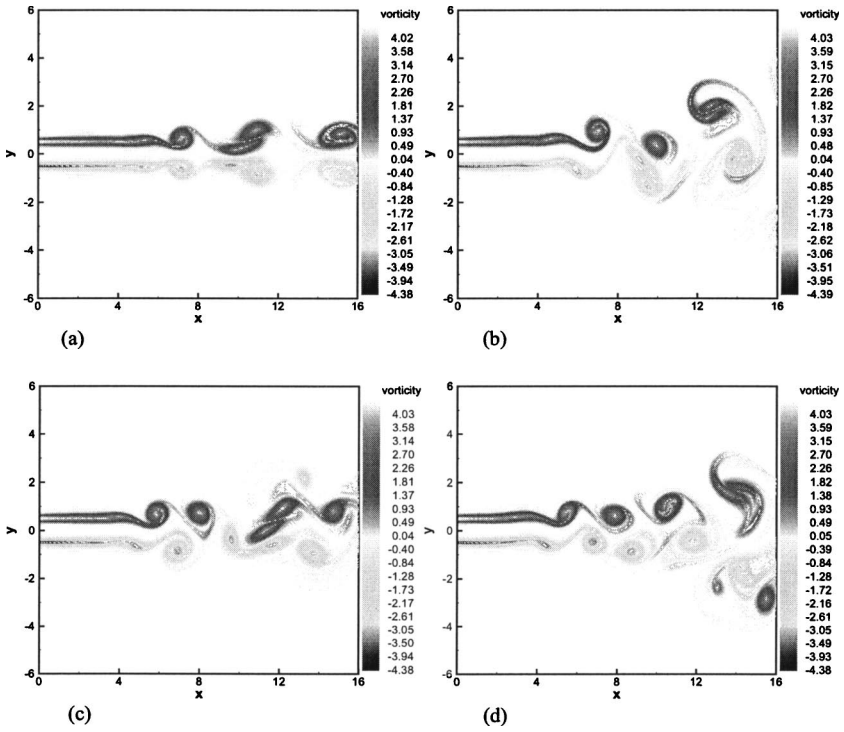

FIG. 3. (Color online) Evolution of vortex structures in the asymmetric mode of flow fields at different nondimensional time t in the fully developed jet flow. (a) $t=79.22$, (b) $t=212.42$, (c) $t=345.62$, and (d) $t=478.82$.

which is the onset of the self-preservation. This result is different from the previous results [9,34]. The delay of the switch position may be associated with the presence of coflow considered in this study. It has been found that the coflow could slow the development of jet flow [35].

The pairing process of three vortex structures is also captured as shown in Fig. 4. First, two roller vortex structures interact with each other, corotate, and pair as shown in Fig. 4(a). Then, the paired vortex structures interact with the third roller vortex structures. They come close to each other, corotate, coencircle as shown in Figs. 4(b) and 4(c), and finally pair to produce a larger vortex structures as shown in Fig. 4(d). This kind of pairing process is related to the consecutively subharmonic resonance.

2. Flow-field variable distribution

For the compressible ideal gas flow considered in this study, the material density is not a constant in the development of flow field. Figure 5 shows the distribution of velocity vector, vorticity, pressure, and density at $t=306.02$. At the

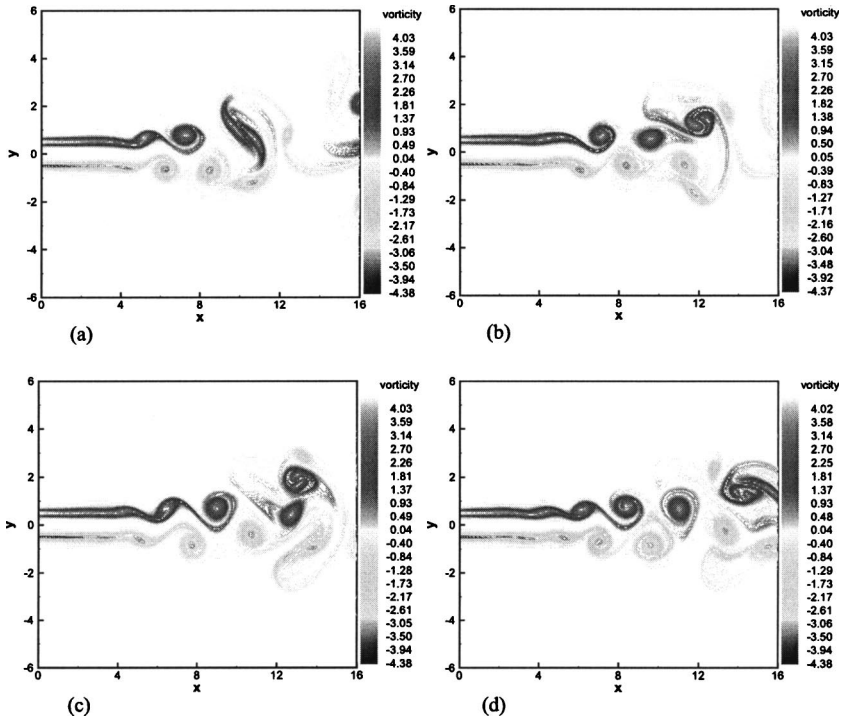

FIG. 4. (Color online) Pairing of three vortex structures at different nondimensional time t. (a) $t=327.62$, (b) $t=331.22$, (c) $t=334.82$, and (d) $t=338.42$.

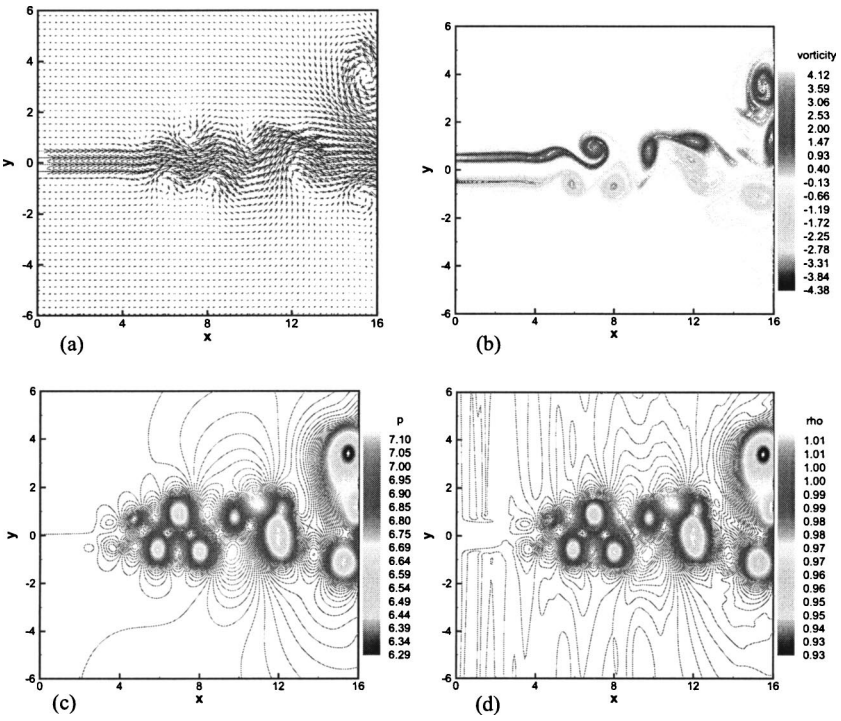

FIG. 5. (Color online) Distribution of fluid flow variables at the nondimensional time of $t=306.02$. (a) Velocity vector, (b) vorticity, (c) pressure, and (d) density.

boundary zones between two vortex structures (vortex braid zones), the velocity vector, pressure, and density are large, but the absolute value of vorticity is low. However, in the vortex core zones, the smaller velocity vector results in the higher absolute value of vorticity and smaller pressure and density. These results are associated with the "stretching" mechanism of large-scale vortex structures in the flow field and may have an effect on the dispersion of particles. In addition, the change of density is very small in the flow field due to the small convection Mach number.

3. Flow-field statistic results

Figure 6 shows the profiles of mean streamwise and lateral velocities along the lateral direction at different streamwise positions. The predicted results are compared with experimental data [36]. b is the half-width of jet velocity, which is the distance from the jet centerline to the point where the mean streamwise velocity excess $U_e=U-U_2$ is half of the centerline velocity excess $\Delta U_c=U_n-U_2$. U_m is the nondimensional mean streamwise velocity $U_e/\Delta U_c$, and V_m is the nondimensional mean lateral velocity, $V/\Delta U_c$.

The initial flat profile of streamwise velocity changes its shape to the sharp velocity profile gradually along the streamwise direction. The sharp velocity profile appears first at the position of $x/d=6.67$, which is close to the first merging point of two side shear layers, suggesting that the mean streamwise velocity reaches the self-similar status as shown in Fig. 6(a). Furthermore, the mean streamwise velocities agree very well with the generalized results [3] and experimental data [36] showing the validity of this direct numerical simulation.

As to the mean lateral velocity profiles, the first position at which the mean lateral velocity profile begin to exhibit self-similar behavior is $x/d=7.33$ as shown in Fig. 6(b). It indicates that the profiles of mean lateral velocity adjust more slowly to the self-similar shape than the profiles of mean streamwise velocity. Good agreement with experimental data [36] is also observed.

Figure 7 shows the profiles of turbulent intensities along the lateral direction at different streamwise positions. $T_x(=\sqrt{\overline{u'^2}}/\Delta U_c)$ and $T_y(=\sqrt{\overline{v'^2}}/\Delta U_c)$ denote the streamwise and lateral fluctuation intensities, respectively. In the region of $x/d<7.0$, the fields of turbulent fluctuation grow fast because the mean velocity profile adjust its initial flat profile to the sharp one. After $x/d=7.0$, the turbulent fluctuation intensities increase slowly because the mean velocity profiles reach self-similar status. As expected, there are two peaks of turbulent intensities at about $y/b=\pm 1.0$, where the shear between fluids is the strongest. The spread of peaks and the transit of the sharp profiles to the more flat ones of turbulent intensities indicate that there is energy transfer between streamwise and lateral fluctuations. Though the mean velocity profiles become self-similar at about the downstream position of $x/d=7.0$, the fluctuation intensity profiles attain self-similar status at about the downstream position of $x/d=10.0$. At this position, the flow field changes its mode from the symmetric pattern to the asymmetric one, and all of the turbulent components are in equilibrium. This is called the self-preserving status [37].

The distribution of Reynolds shear stress in the flow field is depicted in Fig. 8. The Reynolds shear stress is defined as $R_{uv}=\overline{u'v'}/\Delta U_c^2$. The Reynolds shear stress grows very rapidly in the initial region of jet. With the reorganization of fluctuation intensities in the self-similar region of mean velocity profiles, the Reynolds shear stress reaches the self-similar state at the downstream position of $x/d=10.0$, which is similar to the development of turbulent intensity profiles. The numerical results are also in good accordance with experimental data [36].

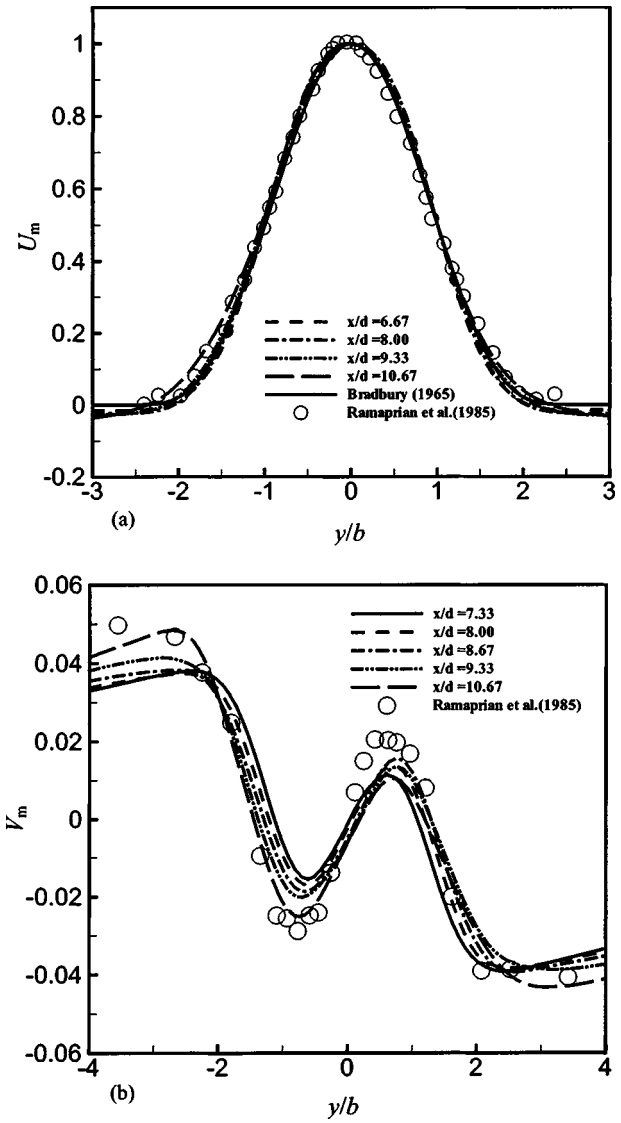

FIG. 6. Distribution of mean velocity profiles along the lateral direction (y). (a) Mean streamwise velocity (U_m) profiles and (b) mean lateral velocity (V_m) profiles.

Figure 9 shows the maximum value of vorticity $w_{\max}$ as a function of time. The value of $w_{\max}$ grows rapidly at the dimensionless time of $t<50$. This corresponds to the time interval at which the symmetric mode is dominant in the development of flow field. At the dimensionless time of $t>80$, the flow field changes its mode to the asymmetric pattern and the maximum value of vorticity begins to fluctuate with the reorganization or destruction of vorticity fields. The fluctuation intensity is quite low and the mean value of $w_{\max}$ is about 4.47.

B. Particle-field results

1. Particle dispersion patterns

The dispersion pattern of particles for different Stokes numbers at non dimensional times of $t=75.62$ and 302.42 are depicted in Figs. 10 and 11, respectively. In order to investigate the relation between the large-scale vortex structures and the dispersion of particles, the vorticity contours at the nondimensional times of $t=75.62$ and 302.42 are also included in these figures. As shown in Fig. 10, all the particles disperse symmetrically over the whole region along the centerline of the jet when the symmetric mode governs the development of flow field. When the flow field changes its

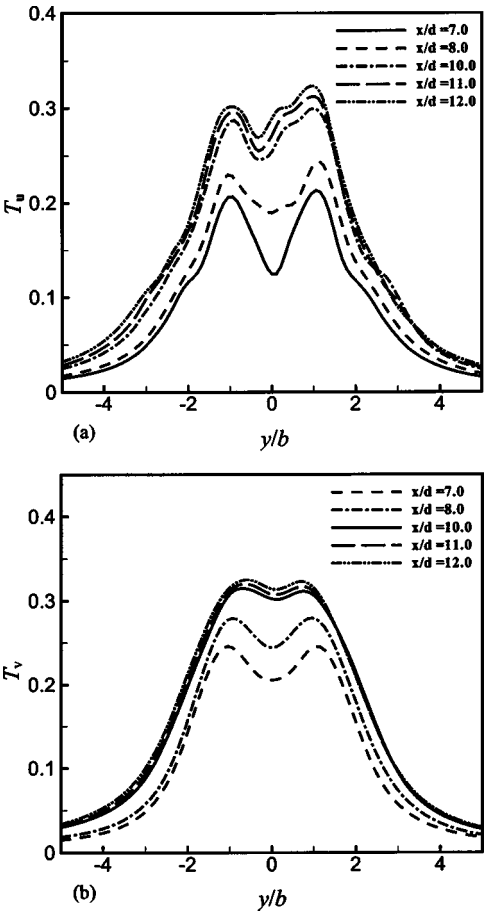

FIG. 7. Distribution of turbulent fluctuation intensity profiles along the lateral direction (y). (a) Streamwise fluctuation intensity (T_u) and (b) lateral fluctuation intensity (T_v).

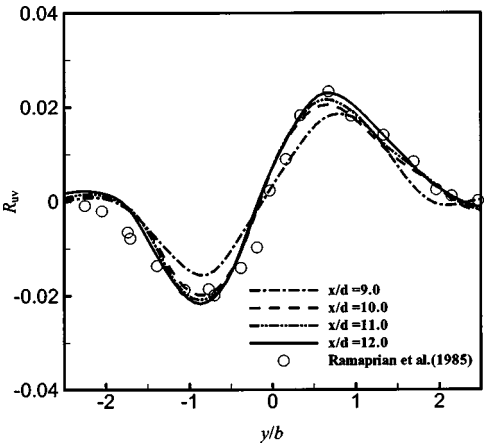

FIG. 8. Distribution of the Reynolds shear stress (R_{uv}) profiles along the lateral direction (y) at different streamwise locations.

shape to the asymmetric mode, the distribution of particles also becomes asymmetric.

The pattern of particle dispersion depends on the Stokes number. When the Stokes number is low at a value of 0.01, the pattern of particle distribution shows good visualization of vortex structures. In this case, the particles follow the fluid closely because they can respond to the flow rapidly due to their much smaller aerodynamic response time. However, when the Stokes number increases to 50, as shown in Figs. 10(f) and 11(f), the dispersion of particles along the lateral direction is very little. As a result most of the particles penetrate through the leading vortex structures and move toward the downstream along nearly rectilinear paths. This pattern of particle distribution indicates that the particle motion does not depend much on the vortex structure in the flow field when the Stokes number is relatively large. The reason is that the aerodynamic response time of these particles is quite longer than the characteristic time scale of the large-scale vortex structures in the flow field. As a result the particles respond very slowly to the change in the flow field. These

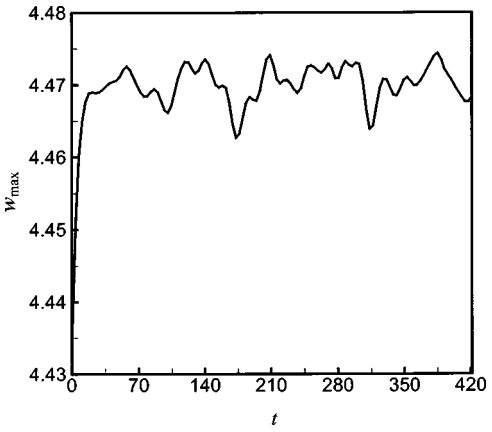

FIG. 9. Time history of the maximum value of vorticity (w_{max}) in the flow field.

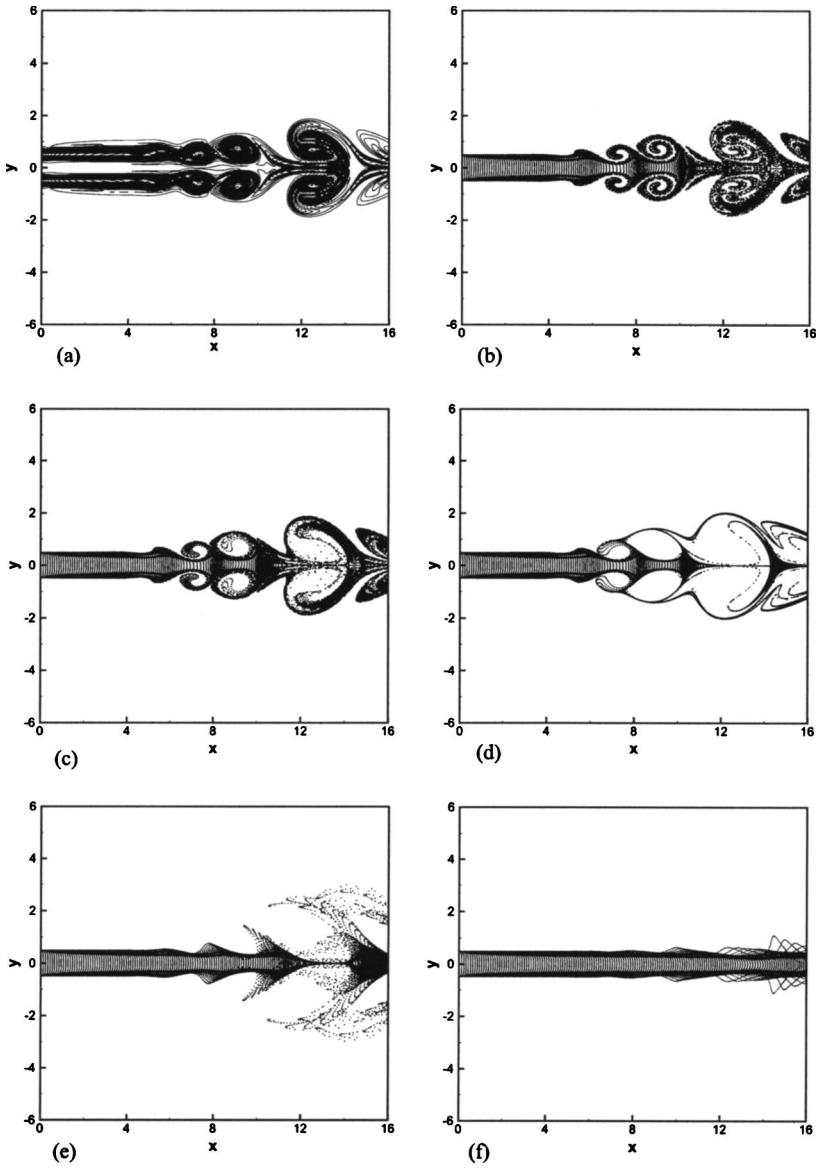

FIG. 10. Dispersion pattern of particles for different Stokes numbers St at nondimensional time of $t=75.62$. (a) Vorticity contour, (b) St=0.01, (c) St=0.1, (d) St=0.5, (e) St=10, and (f) St=50.

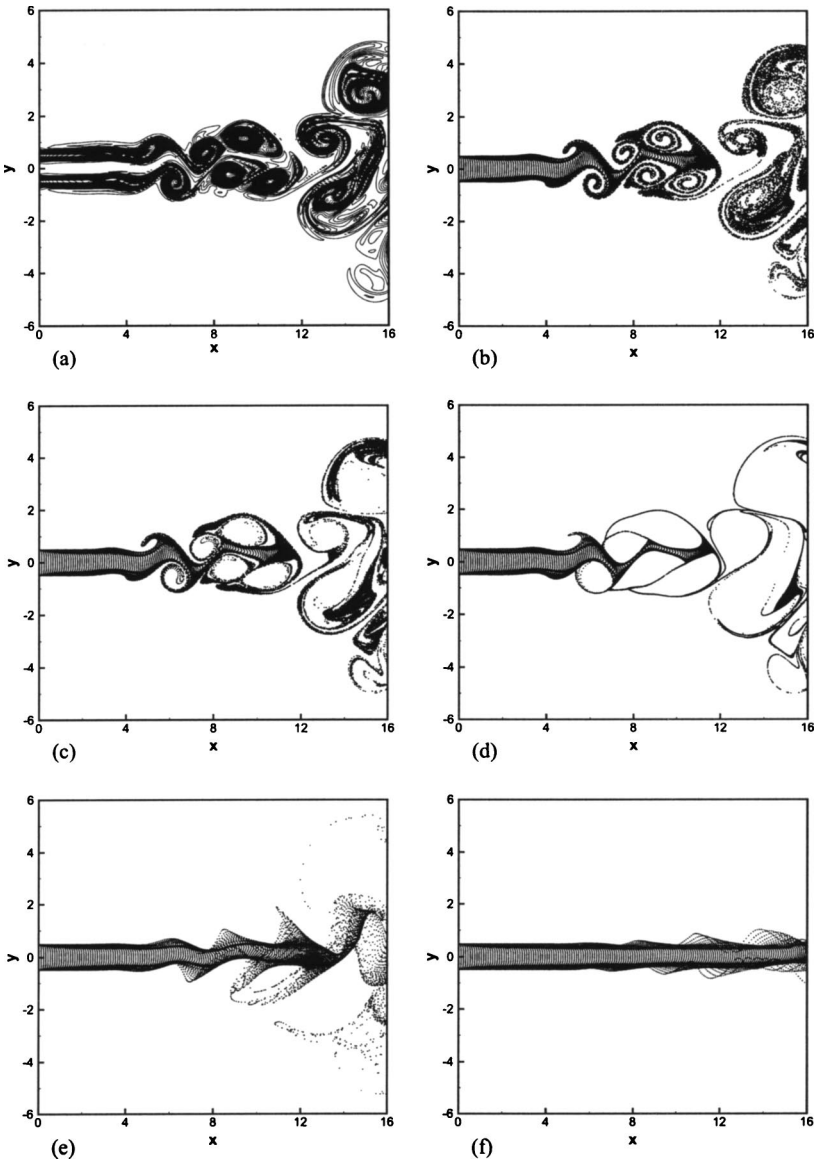

FIG. 11. Dispersion pattern of particles for different Stokes numbers St at nondimensional time of $t=302.42$. (a) Vorticity contour, (b) St=0.01, (c) St=0.1, (d) St =0.5, (e) St=10, and (f) St=50.

patterns of particle dispersion have been often observed in the gas-particle two-phase flow in the free shear flows, such as the mixing layer [38,39] and plane wake [31,40].

However, when the Stokes number has intermediate values of 0.5 and 5, the pattern of particle dispersion is interesting. Nearly all the particles are thrown out of the vortex core region and are concentrated on the vortex boundaries to form highly organized distribution. We call it the quasicoherent structure of particle dispersion. The outline of quasicoherent structure of particle dispersion is very clear, but the scope is larger than that of the corresponding vortex structures because the particles are dispersed more quickly than the fluid. It is clearly observed that the particles are assembled largely in the thin regions that connect opposite sign vortex structures with the lower vorticity. Especially, the particles are largely focused on the end of the thin regions that link multiple large-scale vortex structures. This concentration of particles is not global but local phenomena, which comes from the stretching and folding of particles among the adjacent vortex structures. It is worth noting that the characteristics of particle dispersion in the jet at the intermediate particle Stokes numbers are different from those in the plane mixing layers and wakes. In the mixing layers, the dispersion patterns of particles seem to be associated with the stretching and folding mechanisms [38], but there is no apparent focusing effect of particles due to the lack of interaction between two shear layers. In the plane wake, the pairing phenomena of vortex structures are rare and the focusing characteristics of particle dispersion are global [31]. However, in the plane jets, there exist both the significant vortex pairing phenomena and the strong interactions between the opposite-sign vortex structures in each side shear layer. This unique nature of flow field results in the particular dispersion pattern of particles.

The dispersion pattern of particles at the Stokes number of 0.1 has the intervenient characteristics, comparing with that at the Stokes numbers of 0.01 and 0.5. More dense distribution of particles is observed near the boundaries of vortex structures. But, few particles exist in the core regions of vortex structure. When the Stokes number increases to 10, the particle dispersion along the lateral direction decreases greatly, compared to that at the Stokes numbers of 0.1 and

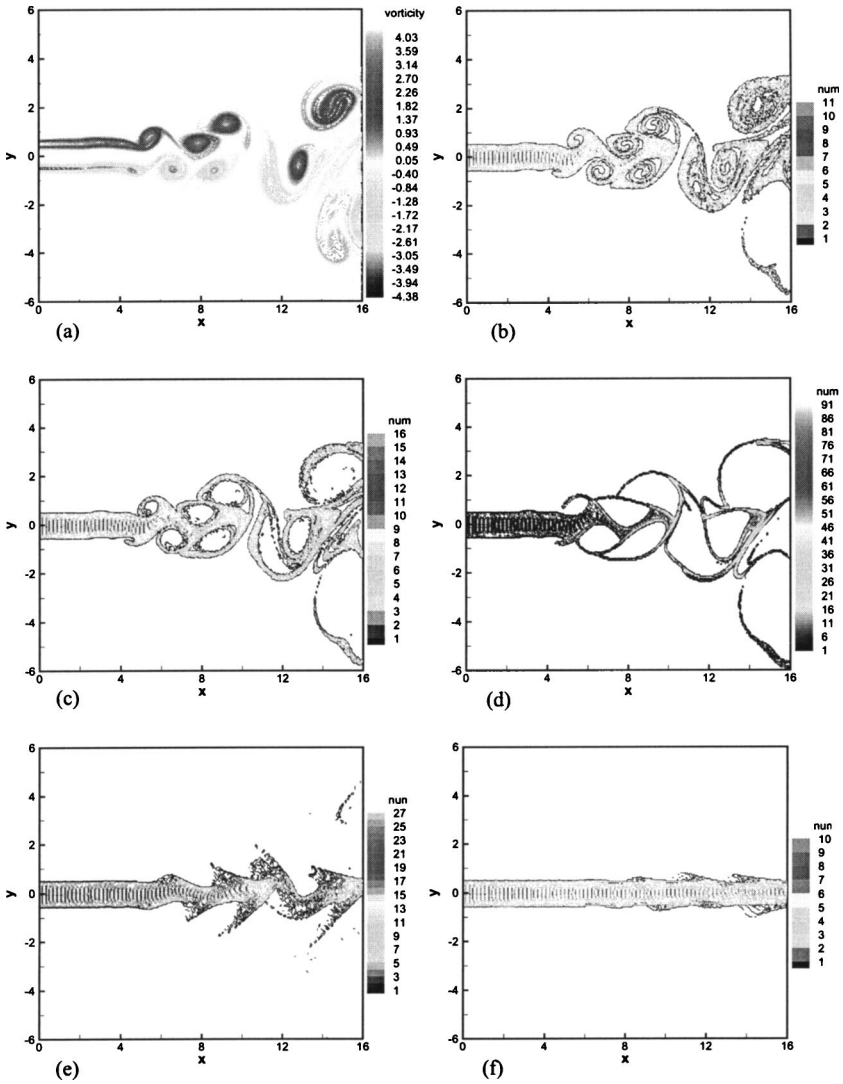

FIG. 12. (Color online) Distribution of particle number density for different Stokes numbers St at nondimensional time of $t=252.02$. (a) Vorticity contour, (b) St=0.01, (c) St=0.1, (d) St=0.5, (e) St=10, and (f) St=50.

0.5. The dispersion pattern of particles at the Stokes number of 10 shows a "fish-bone" shape with the moderate particle dispersion.

To quantify the distribution of particles for different Stokes numbers in the flow field, the number density of particles is calculated. The particle number density is defined as the number of particles located in each grid at some time to describe the distribution of particle concentration in the flow field. The contours of particle number density for different Stokes numbers at $t=252.02$, which are coupled with the vorticity distribution, are shown in Fig. 12. The number density of particles at the Stokes numbers of 0.01 and 50 is lower and shows even distribution, suggesting that these two kinds of particles distribute uniformly in the flow field due to much smaller and much larger aerodynamic response time, respectively. At the intermediate Stokes number of 0.5, the number density of particles has much higher values in the outer regions with large-scale vortex structures. Particularly, in the converging regions of boundaries at which multiple vortex structures are connected, the particle number density becomes extremely high due to the local focusing phenomena of particles. This local focusing process is related to the successive vortex pairing mechanism and strong interactions between two shear layers. It should be pointed out that the fluid pressure and density are higher in these regions, but the effect of flow pressure and density on particle dispersion is much smaller than that of coherent structures of fluid flow. The number density of particles at the Stokes number of 0.1 is also intervenient, comparing with that at the Stokes numbers of 0.01 and 0.5. When we increase the Stokes number to 10, the moderate nonuniformity in the distribution of particle concentration is observed. These quantified results coincide well with qualitative results.

2. Potential particle dispersion mechanism

To reveal the mechanism of the particle dispersion pattern observed above, the relative slip velocity vector V_r, which represents the difference between the particle and fluid velocity vectors at the same time, is defined and computed. Figures 13 and 14 show the vorticity contour and relative velocity vectors for different Stokes numbers at $t=46.82$ and 324.02, respectively. The flow fields at $t=46.82$ are symmetric, whereas those at $t=324.02$ are symmetric. When the Stokes number is small as St=0.01, the relative slip velocity vector has very small values and is distributed uniformly in the flow field, showing that these particles can disperse al-

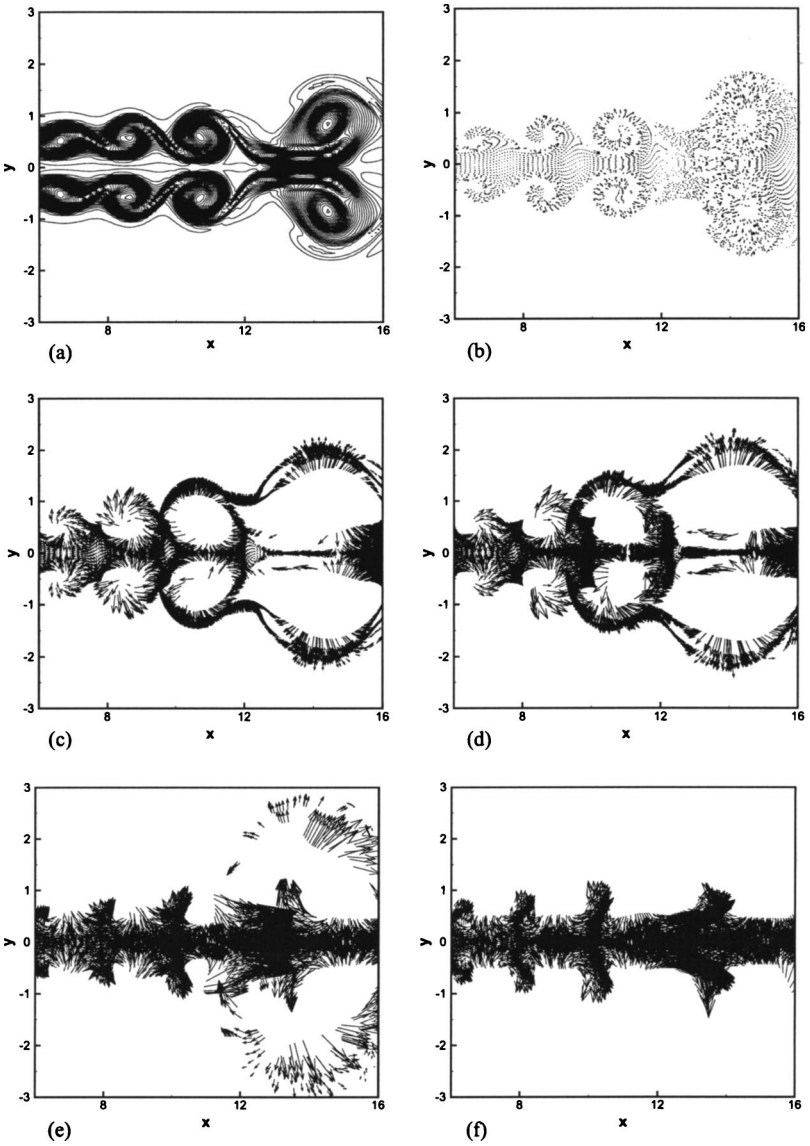

FIG. 13. Distribution of relative velocity vector for different Stokes numbers St at nondimensional time of $t=46.82$. (a) Vorticity contour, (b) St=0.01, (c) St=0.5, (d) St=5, (e) St=10, and (f) St=50.

most as fast as the fluid. When the Stokes numbers are as large as St=10 and 50, only a few particles have the large relative slip velocity along the lateral direction and most of the particles have much larger relative slip velocity along the streamwise direction. It means that these particles disperse very little along the lateral direction and mainly follow a linear path to the downstream with high velocity.

However, when the Stokes numbers are intermediate, such as St=0.5 and 5, the distribution of relative slip velocity vectors is extraordinary. There exist a series of saddles in the distribution of relative slip velocity vectors at the middle positions of boundaries that link two opposite-sign vortex structures and at the converging core regions that connect multiple vortex structures. In these saddle regions, the magnitude of fluid velocity is very high, but the magnitude of vorticity is quite low. When the flow field is in a symmetric mode, the relative slip velocity vector is concentrated on the vortex braid regions that connect two roller vortex structures with the same sign. This is associated with the consecutive linear arrangement of saddles because of the interactions between the vortex structures with the same and opposite signs. In this case, the local focusing process of particles happens due to the folding phenomena of particles into the vortex braid regions from the adjacent vortex structures. However, when the flow field is asymmetric, the saddles in the converging core regions, which are formed by connecting multiple neighboring vortex structures, are destroyed. So the focusing process of particles occurs in the whole converging regions that link three vortex structures. In the pairing process of two vortex structures, the particles are folded into the thin boundary layer first, and then the stretching process of particles follows. When the particles assembled in the thin boundary layer begin to stretch, the particles deviate from the central position of boundary to the opposite directions with the same magnitude of the relative slip velocity. In addition, the magnitude of the relative slip velocity vector at the intermediate Stokes numbers is considerably large, showing that the dispersion speed of these particles is faster than the fluid.

It seems that the relative slip velocity vector can reflect the dispersion mechanism of particles well. From these results, we can see that the dispersion patterns of particles at

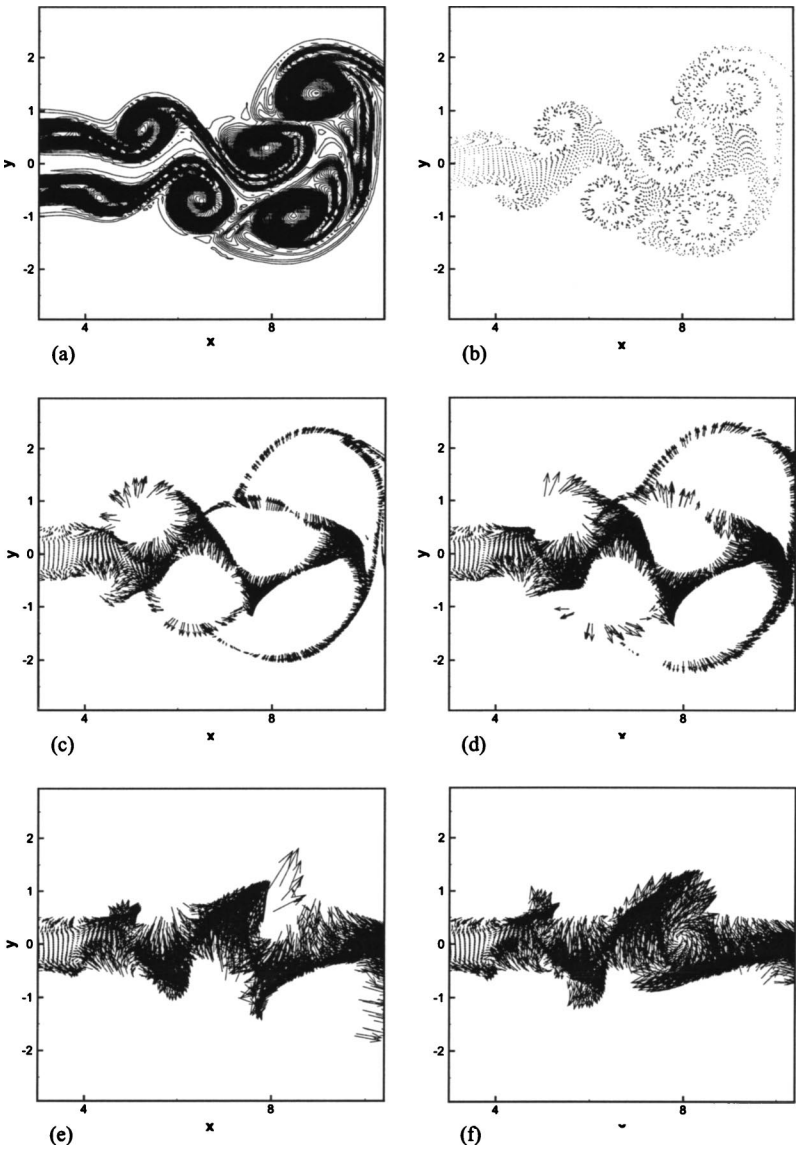

FIG. 14. Distribution of relative velocity vector for different Stokes numbers St at nondimensional time of $t=324.02$. (a) Vorticity contour, (b) St=0.01, (c) St=0.5, (d) St=5, (e) St =10, and (f) St=50.

the intermediate Stokes numbers in the coflow plane jet is different from those in the plane mixing layers and wakes. The mechanism depends closely on the strong interactions between two side shear layers and the successive pairing process of vortex structures with the same sign. This kind of particle dispersion characteristics can be described as the local-focusing effect of particle dispersion.

3. Quantitative particle dispersion

In order to describe the uniform degree of particle distribution, the root mean-square function of the number of particles per cell over the whole field N_{rms} is defined as follows:

$$N_{\mathrm{rms}}(t) = \sqrt{\frac{\sum_{i=1}^{n_t} n_i^2(t)}{n_t}} \tag{11}$$

where n_t is the total computational cell number and $n_i(t)$ is the number of particles in the ith cell at time t.

Figure 15 depicts the development of N_{rms} for different

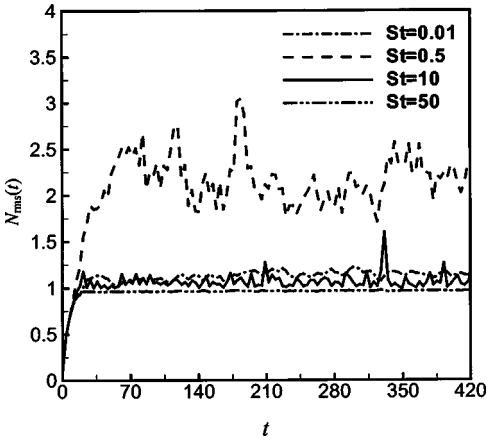

FIG. 15. Time histories of root mean square function $N_{\mathrm{rms}}(t)$ of the number of particles per cell for different Stokes numbers.

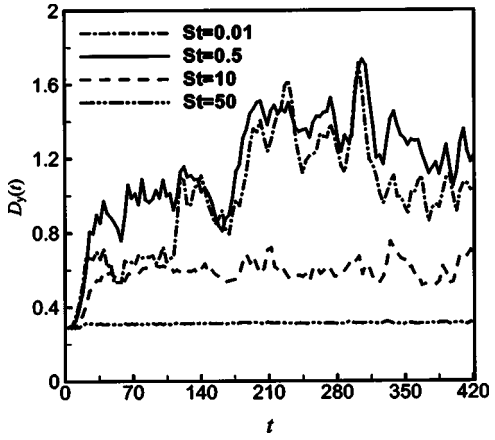

FIG. 16. Time histories of lateral dispersion function $D_y(t)$ of particles for different Stokes numbers.

Stokes numbers. It is well known that large-scale structures have a significant affect on the dispersion of particles, when the particle aerodynamic response time scale has the same order as the characteristic time scale of large-scale organized flow structures. Therefore, as shown in Fig. 15, the particles with the Stokes numbers of 0.5 apparently have the larger values of N_{rms}. The values of N_{rms} increase during the initial period of its time history, and then maintain a mean value of 2.0 with the fluctuating amplitude around 0.5 when the flow field changes its distribution to the asymmetric mode. The larger fluctuation of N_{rms} is associated with the local-focusing effect of particles at the intermediate Stokes numbers. In these cases, the particles are distributed very unevenly in the flow field. But, for the particles with the smaller or larger Stokes numbers at St=0.01 or 10 and 50, the values of N_{rms} increase first, and then reach the value of about 1.0 with very small fluctuation, suggesting that these particles are distributed evenly in the flow field. These results agree well with the analysis results for the distribution of particles mentioned above.

To study the dispersion level of particles along the lateral direction due to the effect of large-scale vortex structures quantitatively, the dispersion function of particles in the lateral direction (y) is introduced. The dispersion function D_y is expressed as follows:

$$D_y(t) = \sqrt{\frac{\sum_{i=1}^{n_y(t)} [Y_i(t) - Y_m(t)]^2}{n_y(t)}} \qquad (12)$$

where $n_y(t)$ is the total number of particles distributed in the whole flow field at time t, $Y_{\mathrm{i}}(t)$ is the particle displacement along the lateral direction at the same time, and $Y_m(t)$ is a mean value for all particles.

Figure 16 shows the development of lateral dispersion function of particles for different Stokes numbers. At first, the particles at the Stokes number 0.01 exhibit more dispersion in the lateral direction. When the Stokes number has the order of unity as St=0.5, the particles disperse more in the flow field due to the development of large-scale structures and the preferential effect of these structures on these particles [41]. However, when the Stokes number is large, such as St=10 and 50, the extent of dispersion is low and D_y varies smoothly, especially for the particles at St=50. As a whole, the dispersion function along the lateral direction for the particles in the range of intermediate Stokes numbers has the largest value with large fluctuation due to the local-focusing effect. These results are consistent partly with the results obtained using DNS for the flow in the mixing layer [32,39].

IV. CONCLUSIONS

DNS for the gas-particle two-phase flow in the compressible, turbulent plane jet flow is performed. We stress on the evolution of large-scale vortex structures and the different patterns of particle dispersion in the near fields of the nozzle. The results show that the transition of flow field from the symmetric mode to the asymmetric mode occurs at the downstream position after the two shear layers are first merged and at the upstream position of overall self-preserving region. The pairing process among three vortex structures is captured. The statistics results for the mean velocity and Reynolds shear stress agree well with the previous experimental results. The profiles of mean velocity reach the self-similar status at the more upstream position than those of Reynolds shear stress and turbulent intensities. When the Stokes number has the order of unity, particles are observed to come together near the outer edges of large-scale vortex structures to form quasicoherent dispersion structures of particle. The local-focusing process of particles happens in the converging region that connects multiple vortex structures. So these particles are distributed very unevenly in the flow field and disperse more along the lateral direction. When the Stokes number is small as St=0.01, particles follow the fluid flow closely and have considerable dispersion along the lateral direction. But, the concentration of particles is low and their distribution is even. When the Stokes number is large as St=10 and 50, particles tend to disperse much less along the lateral direction and to pass though the vortex structures with even distribution.

ACKNOWLEDGMENTS

The authors gratefully acknowledge the support of this research by the Special Funds for Major State Basic Research Projects (Grant No. G19990222-05) and the Key Foundations of the National Natural Science of People's Republic of China (Grant No. 50236030). In addition, this work was partially supported by the Brain Korea 21 project and National Research Laboratory Project sponsored by the Korean government. We appreciate it.

[1] M. L. Albertson, Y. B. Dai, R. A. Jenson, and H. House, Trans. Am. Soc. Civ. Eng. **115**, 639 (1950).
[2] D. R. Miller and E. W. Comings, J. Fluid Mech. **3**, 1 (1957).
[3] L. J. S. Bradbury, J. Fluid Mech. **23**(1), 31 (1965).
[4] E. Gutmark and I. Wygnanski, J. Fluid Mech. **73**(3), 465 (1976).
[5] V. W. Goldschmidt and P. Bradshaw, Phys. Fluids **16**(3), 354 (1973).
[6] K. W. Everitt and A. G Robins, J. Fluid Mech. **88**(3), 563 (1978).
[7] Cervantes de J. C. Gortari and V. W. Goldschmidt, J. Fluids Eng. **103**(1), 119 (1981).
[8] J. W. Oler and V. W. Goldschmidt, J. Fluid Mech. **123**, 523 (1982).
[9] F. O. Thomas and V. W. Goldschmidt, J. Fluid Mech. **163**, 227 (1986).
[10] T. Zhou, B. R. Pearson, and R. A. Antonia, Fluid Dyn. Res. **28**, 127 (2001).
[11] Y. Dai, T. Kobayashi, and N. Taniguchi, JSME Int. J., Ser. A **37**(2), 242 (1994).
[12] S. Stanley and S. Sarkar, Theor. Comput. Fluid Dyn. **9**, 121 (1997).
[13] W. K. Melville and K. N. C. Bray, Int. J. Heat Mass Transfer **22**, 647 (1979).
[14] J. N. Chung and T. R. Troutt, J. Fluid Mech. **186**, 199 (1988).
[15] Y. Hardalupas, A. M. P. K. Taylor, and J. H. Whitelow, Proc. R. Soc. London, Ser. A **426**, 31 (1989).
[16] S. Yuu, K. Ikeda, and T. Umekage, Colloids Surf., A **109**, 13 (1996).
[17] J. Despirito and L. P. Wang, Int. J. Multiphase Flow **27**, 1179 (2001).
[18] S. Yuu, T. Ueno, and T. Umekage, Chem. Eng. Sci. **56**, 4293 (2001).
[19] K. W. Thompson, J. Comput. Phys. **68**, 1 (1987).
[20] N. A. Adams, Theor. Comput. Fluid Dyn. **12**, 109 (1998).
[21] F. Q. Hu, J. Comput. Phys. **129**, 201 (1996).
[22] F. Q. Hu, J. Comput. Phys. **173**, 455 (2001).
[23] J. B. Freund, S. K. Lele, and P. Main, AIAA J. **38**(11), 2023 (2003).
[24] T. J. Poinsot and S. K. Lele, J. Comput. Phys. **101**, 104 (1992).
[25] D. H. Rudy and J. C. Strikwerda, J. Comput. Phys. **36**, 55 (1980).
[26] S. K. Lele, J. Comput. Phys. **103**, 16 (1992).
[27] M. H. Carpenter, D. Gottlieb, and S Abarbanel, J. Comput. Phys. **108**, 272 (1993).
[28] M. H. Carpenter and C. A. Kennedy, NASA TM 109112, 1994 (unpublished).
[29] J. R. Fan, K. Luo, Y. Q. Zheng, H. H. Jin, and K. F. Cen, Phys. Rev. E **68**, 036309 (2003).
[30] R. Chein and J. N. Chung, AIChE J. **34**, 946 (1988).
[31] L. Tang, F. Wen, Y. Yang, C. T. Crowe, J. N. Chung, and T. R. Troutt, Phys. Fluids A **4**, 2244 (1992).
[32] W. Ling, J. N. Chung, T. R. Troutt, and C. T. Crowe, J. Fluid Mech. **358**, 61 (1998).
[33] M. R. Maxey and J. J. Riley, Phys. Fluids **26**, 883 (1983).
[34] R. A. Antonia, L. W. B. Browne, S. Rajagopalan, and A. J. Chambers, J. Fluid Mech. **134**, 49 (1983).
[35] R. S. Reichert and S. Biringen, Appl. Acoust. **62**, 1049 (2001).
[36] B. R. Ramaprian and M. S. Chandrasekhara, ASME J. Fluids Eng. **107**, 264 (1985).
[37] I. Wygnanski and H. Fiedler, J. Fluid Mech. **38**, 577 (1969).
[38] F. Wen, N. Kamalu, J. N. Chung, C. T. Crowe, and T. R. Troutt, J. Fluids Eng. **114**, 657 (1992).
[39] J. R Fan, Y. Q. Zheng, J. Yao, and K. F. Cen, Proc. R. Soc. London, Ser. A **457**, 2151 (2001).
[40] Y. Yang, C. T. Crowe, J. N. Chung, and T. R. Troutt, Int. J. Multiphase Flow **26**, 1583 (2000).
[41] J. K. Eaton and J. R. Fessler, Int. J. Multiphase Flow **20**, 169 (1994).